The Astrophysical Journal, 658:1164–1172, 2007 April 1

OBSERVATIONS OF HERBIG Ae DISKS WITH NULLING INTERFEROMETRY[1]

Wilson M. Liu,[2] Philip M. Hinz, Michael R. Meyer, Eric E. Mamajek,[3] William F. Hoffmann, Guido Brusa, Doug Miller, and Matthew A. Kenworthy
Steward Observatory, University of Arizona, Tucson, AZ; wliu@as.arizona.edu
Received 2006 September 25; accepted 2006 December 12

ABSTRACT

We present the results of 10 μm nulling interferometric observations of 13 Herbig Ae stars using the Magellan I (Baade) and the MMT 6.5 m telescopes. A portion of the observations was completed with the adaptive secondary at the MMT. We have conclusively spatially resolved 3 of the 13 stars, HD 100546, AB Aur, and HD 179218, the latter two recently resolved using adaptive optics in combination with nulling interferometry. For the resolved objects we find that the 10 μm emitting regions have a spatial extent of 15–30 AU in diameter. We also have some evidence for resolved emission surrounding an additional two stars (V892 Tau and R CrA). For those objects in our study with mid-IR SEDs in the classification of Meeus and coworkers, we find that the group I objects (those with constant to increasing mid-IR flux) are more likely to be resolved, within our limited sample. This trend is evident in correlations in the inferred disk sizes versus the submillimeter SED slope and disk size versus fractional infrared luminosity of the systems. We explore the spatial distribution and orientation of the warm dust in the resolved systems and constrain physical models that are consistent with their observational signatures.

Subject headings: circumstellar matter — instrumentation: adaptive optics — stars: pre–main-sequence — techniques: interferometric

1. INTRODUCTION

Circumstellar disks have now been observed surrounding numerous pre–main-sequence (PMS) stars of intermediate mass. Herbig Ae (HAe) stars are of particular interest, as they are the evolutionary precursors to stars such as Vega, which are known to harbor solid material in their circumstellar environments. Observations of HAe stars can therefore provide us with information regarding planet formation and the evolution of the circumstellar disks as the stars evolve onto the main sequence. High spatial resolution studies at wavelengths near 10 μm are especially useful, as they can probe material inner parts (a few AU) of these disks, allowing one to directly observe regions where planets could form in the habitable zones of such stars.

Infrared (IR) excess emission from HAe stars was originally explained by the presence of geometrically thin, optically thick disks (Lada & Adams 1992; Hillenbrand et al. 1992), a model that has been modified to include central-star irradiation (Calvet et al. 1991), disk flaring (Chiang & Goldreich 1997; Kenyon & Hartmann 1987), and other structures to explain features in the spectral energy distributions (SEDs), such as an inner hole, inner-wall heating, and self-shadowing (Dullemond 2002; Dullemond et al. 2001). Alternative explanations for circumstellar emission take the form of dusty envelopes or envelope+disk models (Miroshnichenko et al. 1999; Hartmann et al. 1993), as well as optically thin "halos" in combination with disks (Vinković et al. 2003, 2006).

A review of observational results prior to 2000 can be found in Natta et al. (2000). More recently, a study by Meeus et al. (2001, hereafter M01) based on *ISO* spectroscopy of HAe stars suggests that they may be classified into two groups based on the shape of the SED, and explainable by differences in disk geometry. We compare our observational results to the M01 classifications in § 4. Recent years have also seen the growth of interferometric observations of HAe stars (see Millan-Gabet et al. 2001 for a review). Leinert et al. (2004) completed a long-baseline, spectrally resolved survey of seven HAe stars using the Very Large Telescope Interferometer at a wavelength of 10 μm. Their study found the 10 μm emission regions to be 1–10 AU in size and determined a correlation between the mid-IR SED slope and the physical size of the disk, where objects with larger emitting regions had redder SEDs. They have attributed this correlation to differences in disk geometry. Additional interferometric observations of HAe stars have been done in the near-IR and include the studies of Eisner et al. (2003) and Millan-Gabet et al. (2001). Eisner et al. used the Palomar Testbed Interferometer at 2.2 μm and inferred the spatial structure and orientation of the near-IR disks surrounding several stars. In a study using the Infrared Optical Telescope Array, Millan-Gabet et al. successfully resolved several near-IR emitting regions surround HAe stars, establishing a size scale for the near-IR region of 0.5–5.9 AU and finding that the distribution of material surrounding resolved objects (including AB Aur) seems to favor a circularly symmetric geometry. We will compare our results to those of previous interferometric studies in § 4. Observations at longer wavelengths include a millimeter study of HAe stars by Mannings & Sargent (1997) and observations of AB Aur by Marsh et al. (1995).

Nulling interferometry is a technique used to study spatially resolved circumstellar material in the presence of unresolved flux and represents an ideal opportunity to observe the environments of HAe stars. The technique, first proposed by Bracewell (1978), is implemented by overlapping the pupils of two telescopes (or two subapertures on a single-aperture telescope) with an optical path length difference of $\frac{1}{2}\lambda$ between the beams. The result of such a configuration is a sinusoidal transmission function with the functional form

$$T(\theta) = \sin^2(\pi b\theta/\lambda), \quad (1)$$

[1] The results presented here made use of the of MMT Observatory, a jointly operated facility of the University of Arizona and the Smithsonian Institution. This paper also includes data gathered with the 6.5 m Magellan Telescopes located at Las Campanas Observatory, Chile.

[2] Michelson Graduate Fellow.

[3] Currently at Harvard-Smithsonian Center for Astrophysics, Cambridge, MA.

TABLE 1
TARGET LIST

Name	Spectral Type	d (pc)	log Age (Myr)	Group[a]	References
HR 5999	A5–7	210 ± 40	5.7 ± 0.3	...	1, 2, 3, 4
KK Oph	A6	160 ± 30	6.5 ± 0.5	II	5
DK Cha	A	~200	...	...	1, 2
HD 150193	A1	150 ± 30	>6.3	II	1, 3, 4
HD 98922	B9	>540	...	...	1, 3
HD 104237	A4	116 ± 8	6.3 ± 0.1	II	1, 3, 4
51 Oph	A0	131 ± 15	5.5 ± 0.2	II	1, 4, 5
R CrA	B8	~130	...	...	2
AB Aur	A0	144 ± 20	6.4 ± 0.2	I	2, 3, 4, 6
V892 Tau	A6	150 ± 10	>7	...	2, 6
HD 100546	B9	103 ± 7	>7[b]	I	1, 3, 4, 5
HD 163296	A3	122 ± 15	6.6 ± 0.4	II	4, 5
HD 179218	B9	244 ± 55	5.0 ± 0.6	I	4, 5

[a] Meeus et al. (2001) SED group.
[b] HD 100546 attributed to Lower Centaurus–Crux OB association by de Zeeuw et al. (1999) with an association age of 16 Myr (Mamajek et al. 2002).
REFERENCES.—(1) SIMBAD; (2) Hamaguchi et al. 2005; (3) van den Ancker et al. 1998; (4) Perryman et al. 1997; (5) Leinert et al. 2004; (6) Natta et al. 2000 and references therein.

where b is the baseline of the interferometer, λ is the wavelength of observations, and θ is the angular distance from the observed object to the pointing center of the interferometer (Hinz et al. 2001). During observations, the central destructive fringe is placed on the unresolved point source. This allows us to detect spatially resolved emission, effectively isolating it from the unresolved stellar flux. Thus, nulling interferometry provides the necessary contrast to observe faint circumstellar material in the presence of a much brighter star. In observing PMS stars at wavelengths near 10 μm, where the circumstellar emission dominates the stellar flux (often by more than 2 orders of magnitude), isolating the resolved disk emission from the unresolved disk emission gives us valuable information about the spatial distribution of circumstellar dust. This technique can detect material as close to the star as one-quarter of the fringe spacing, where the light is neither suppressed nor enhanced. This corresponds to 0.12″ for the configuration used on the MMT, or 12 AU about a star at 100 pc. This is between 2 and 3 times finer spatial resolution than the diffraction limit at the wavelengths observed in this study (8–13 μm).

In more recent observations at the MMT, nulling interferometry was implemented in combination with the MMT's adaptive optics (AO) secondary mirror. The addition of AO has benefits for nulling. Specifically, wave front aberrations introduced by the atmosphere that might affect the suppression level of the null are significantly reduced or eliminated. The stabilization of the incoming wave front therefore allows us to precisely tune the path length between the arms of the interferometer, allowing for the best possible suppression of light; hence observations are made more efficient (see § 2). In addition, a stable wave front and image allows us to integrate for greater periods of time, making fainter resolved flux detectable. The unique nature of the deformable secondary also has benefits in mid-infrared observations. Since the secondary mirror of the telescope is the deformable mirror, there is no need for an intermediate set of correcting optics between the telescope and science camera. This reduces the number of warm surfaces in the optical path, minimizing background and maximizing throughput. More technical details regarding the MMT adaptive secondary can be found in Brusa et al. (2003).

In § 2 we discuss the target sample and observations, as well as the reduction procedure for nulling interferometric data. In § 3 we present the results of the observations, and we discuss them in the context of models and previous observations in § 4.

2. OBSERVATIONS AND DATA REDUCTION

2.1. *Target Selection*

Targets for this survey were taken from a catalog of Herbig Ae/Be stars by The et al. (1994). The objects were chosen to include stars with a spectral type of B8 or later, as HAe stars have been found to have a significantly higher incidence of circumstellar disks than Herbig Be stars (Natta et al. 2000). All objects (except one, HD 98922) were chosen to be within 250 pc, to ensure our ability to spatially resolve a circumstellar disk, should one be present. All targets also have a 12 μm flux (*IRAS*) greater than 10 Jy, to ensure sensitivity to any resolved emission. A large flux is necessary for non-AO observations, as we are limited to short integration times (see § 2.4). The final sample of 13 stars, along with their stellar characteristics, is shown in Table 1.

Observations of 13 Herbig Ae stars were made in 2001 August and 2002 May at the 6.5 m Magellan I (Baade) telescope at the Las Campanas Observatory, Chile, and in 2002 November, 2004 January, and 2005 June at the 6.5 m MMT at Mount Hopkins, Arizona. On these single-aperture telescopes, nulling interferometry is implemented by dividing the aperture into two identical elliptical subapertures, each 2.5×5 m^2 with a baseline of 4 m. The Bracewell Infrared Nulling Cryostat (BLINC; Hinz 2001) is the interferometer that reimages the primary mirror as two subapertures and recombines the beams with an appropriate path difference. The recombined image is fed to the Mid-Infrared Array Camera 3 (MIRAC3; Hoffmann et al. 1998), which provides the final stop for the image. Observations were taken at 10.3, 11.7, and in a few cases 12.5 μm, each with a bandwidth of 10%, and with a wide 10.6 μm (N band) filter with a 50% bandpass. In addition, observations of HD 100546 taken at Magellan I included direct imaging taken with BLINC-MIRAC at longer wavelengths (18.0 and 24.5 μm).

2.2. *Non-AO Observations*

Observations taken at Magellan and during the 2002 MMT run were done without AO. Without wave front correction, atmospheric

aberrations randomize the path difference between the two arms of the interferometer. Thus data must be taken with short frame times (50 ms) in order to freeze out the seeing effects. In this case, images are taken contiguously in large sets, typically 500 to a set. This number of frames is sufficient to sample the phase between the beams, and thus include several frames with a phase difference close enough to one-half wave that higher order spatial errors dominate the level of residual flux in the focal plane. The images with the best null (destructive interference) and constructive interference in each set are selected in order to evaluate the "instrumental null" (see below). Ten off-source sky frames, used to subtract out the sky background, are taken after each set of frames on-source. For each science object we take several sets of frames, in order to effectively evaluate the null. From the lowest and highest fluxes in each set of frames, we calculate the *instrumental null*, which is defined as

$$N = \mathrm{flux}_{\mathrm{nulled}}/\mathrm{flux}_{\mathrm{constructive}} \quad (2)$$

and expressed as a percentage.

Observations of each science object are followed by 2–4 sets of 500 frames of a point-source (spatially unresolved) calibrator star in order to establish a baseline for goodness of null achieved in the most recent science observations. Calibrator nulls generally ranged between 5% and 15%. We use the null achieved on the calibrator to calculate the *source null*, defined as the difference between the instrumental null on the science object and the calibrator:

$$S = N_{\mathrm{science}} - N_{\mathrm{calibrator}}. \quad (3)$$

This represents the resolved flux as a percentage of the full flux of the target. A source null of zero means that the science object is spatially unresolved.

In addition, observations are taken with different rotations of the interferometer baseline relative to the sky. Typically, two sets of 500 frames are taken at each rotation. This allows us to probe for the presence of an elongated or flattened structure (such as an inclined disk) if resolved emission is detected, which is accomplished in the following manner. The output of the interferometer is a transmission pattern superimposed on the stellar image. This transmission pattern has a sinusoidal functional form shown in § 1, with the destructive interference fringe directly on-axis and aligned perpendicular to the baseline of the interferometer. If a flattened extended structure is present surrounding our science target and the major axis of the emission is aligned parallel to the destructive interference fringe, we would expect a deeper null (smaller N) than when the fringe and the major axis are orthogonal. The resulting dependence of N versus the rotation of the interferometer would be sinusoidal with a period of 180°,

$$S = a + b \sin(\mathrm{P.A.} + \theta). \quad (4)$$

The parameters a, b, P.A., and θ are determined by the size of the emitting region, its inclination, the position angle of its major axis, and rotation of the interferometer baseline, respectively.

2.3. *Observations with AO*

Observations taken in 2004 January and 2005 June at the MMT were done with the AO secondary. As described in § 1, the use of AO significantly increases the efficiency of observations. Since with AO we are able to precisely tune the path difference between the arms of the interferometer, large sets of fast frames to freeze-out atmospheric effects are unnecessary. AO also stabilizes the image, generally resulting in smaller errors in the null. In this case, we take sets of 10 frames (usually ~1 s integration) of the object tuned to destructive interference, followed by 10 frames of the object in constructive interference. Observations of the calibrator are taken in the same manner, with off-source sky frames taken after each destructive-constructive pair. Calibrator nulls typically range between 3% and 6%, indicating an improvement in both null depth and stability compared to non-AO observations.

Table 2 summarizes all observations of science targets, taken with and without AO.

2.4. *Nulling-Data Reduction*

For non-AO observations, each on-source frame is sky subtracted using a sky frame created by median combining the 10 off-source frames taken immediately after the science frames. A custom IDL program is used to extract aperture photometry from each "on" sky-subtracted frame. The aperture size for each set of frames is chosen by determining the radius at which the source flux disappears into the noise. The noise level is assessed in an annular region several pixels wide well outside the aperture. For each set of 500 frames, we identify the frames with the smallest residual flux (best null) and the brightest constructive image. These two frames are used to evaluate the instrumental null. The null for each set of calibrator images is evaluated in an identical way.

For the frames taken with AO, the best destructive frame in each set is determined using aperture photometry in a manner identical to the non-AO procedure described above. The instrumental null is determined by using the best nulled image and a median-combined composite image of the constructive frames. Instrumental nulls for calibrator stars, taken in between science objects, were evaluated in an identical manner.

Source nulls were evaluated for all data by subtracting the instrumental null of the calibrator from the instrumental null achieved on the science object. A table of instrumental, calibrator, and source nulls and errors is shown in Table 3. The values of the nulls represent an average of the data sets taken at each wavelength and position angle, and errors are the 1 σ dispersion in the values.

3. RESULTS

Out of 13 objects observed, we have conclusively resolved three of the objects, HD 100546 (at three different wavelengths and five different rotations), AB Aur (at one wavelength and five different rotations), and HD 179218 (at one wavelength and two rotations). In addition, we have marginally resolved (at about the 2.5 σ level) two stars, V892 Tau and R CrA. Source nulls for all objects can be found in Table 3.

One may note that source nulls are negative at a significant level (>2 σ) for one set of data. Negative source nulls are unphysical; hence the appearance here necessitates an explanation. The negative value for the set in question (HD 98922; 11.7 μm) can be attributed to an inaccurate measurement of the calibrator null taken immediately after the science object. Analysis of the calibrator images shows a slightly "dual peaked" image of the star, indicating a slight misalignment in the beams of the interferometer and/or a temporary degradation in observing conditions (i.e., bad seeing). This results in a poor null (abnormally large value) for the calibrator null, hence a negative value for a source null. It is important to note that a poor null in the calibrator cannot result in a false positive detection of resolved material, and any detections of resolved emission are checked to ensure that they are not a result of poor seeing or misalignment. The negative

TABLE 2

SUMMARY OF OBSERVATIONS

Observation Set	λ (μm)	Number of Frames	Integration per Frame (s)	P.A. (or Rotation)[a] (deg)	Telescope	Reference
HR 5999:						
1–2	11.7	1000	0.5	−165 (rotation)	Magellan	1
3–4	11.7	1000	0.5	110 (rotation)	Magellan	1
KK Oph:						
5–6		1000	0.5	−150 (rotation)	Magellan	1
7–8	11.7	1000	0.5	120 (rotation)	Magellan	1
DK Cha:						
9–10	11.7	1000	0.45	−170 (rotation)	Magellan	1
HD 150193:						
11–12	11.7	1000	0.45	145 (rotation)	Magellan	1
	10.3	500	0.5	97	MMT	2
HD 98922:						
13–14	11.7	1000	0.55	−40 (rotation)	Magellan	1
15–16	10.3	1000	0.55	−40 (rotation)	Magellan	1
HD 104237:						
17–18	11.7	1000	0.55	−60 (rotation)	Magellan	1
19–20	10.3	1000	0.55	−60 (rotation)	Magellan	1
51 Oph:						
20–21	11.7	1000	0.11	135 (rotation)	Magellan	1
22	11.7	500	0.11	45 (rotation)	Magellan	1
R CrA:						
23–24	11.7	1000	0.11	0 (rotation)	Magellan	1
	11.7	1000	0.11	30 (rotation)	Magellan	1
AB Aur:						
25–27	10.3	60	1.0	170	MMT AO	3
28–30	10.3	60	1.0	107	MMT AO	3
31–33	10.3	60	1.0	71	MMT AO	3
34–36	10.3	60	1.0	131	MMT AO	3
37–39	10.3	60	1.0	4	MMT AO	3
V892 Tau:						
40–41	11.7	1000	0.5	164	MMT	3
42–43	11.7	1000	0.5	116	MMT	3
44–46	10.3	60	1.0	160	MMT AO	3
HD 100546:						
47–48	10.3	1000	0.5	−80 (rotation)	MMT	4
49–50	10.3	1000	0.5	−50 (rotation)	MMT	4
51–52	10.3	1000	0.5	−24 (rotation)	MMT	4
53–54	10.3	1000	0.5	10 (rotation)	MMT	4
55–56	10.3	1000	0.5	40 (rotation)	MMT	4
57–58	11.7	1000	0.5	−80 (rotation)	MMT	4
59–60	11.7	1000	0.5	−50 (rotation)	MMT	4
61–62	11.7	1000	0.5	−24 (rotation)	MMT	4
63–64	11.7	1000	0.5	10 (rotation)	MMT	4
65–66	11.7	1000	0.5	40 (rotation)	MMT	4
67–68	12.5	1000	0.5	−80 (rotation)	MMT	4
69–70	12.5	1000	0.5	−50 (rotation)	MMT	4
71–72	12.5	1000	0.5	−24 (rotation)	MMT	4
73–74	12.5	1000	0.5	10 (rotation)	MMT	4
75–76	12.5	1000	0.5	40 (rotation)	MMT	4
HD 163296:						
77	10.3	500	0.5	94	MMT	2
78	10.3	500	0.5	10	MMT	2
HD 179218:						
79	10.3	500	0.5	162	MMT	2
80	10.3	500	0.5	87	MMT	2
81–89	10.6	90	1.0	50	MMT AO	1
90–98	10.6	90	1.0	60	MMT AO	1
99–104	10.6	60	1.0	99	MMT AO	1
105–110	10.6	60	1.0	103	MMT AO	1

[a] The P.A. probed by the nulling observation depends on both the rotation of the interferometer baseline and the parallactic angle of the object when observed. For objects denoted "rotation," the parallactic angle was not recorded, so the rotation of the interferometer (degrees from an arbitrary position) is noted so that the reader can estimate the relative value of the P.A. for observations of each object.

REFERENCES.—(1) This paper; (2) Hinz et al. 2001; (3) Liu et al. 2005; (4) Liu et al. 2003.

TABLE 3
INSTRUMENTAL AND SOURCE NULLS

Star	Instrumental Null (%)	Calibrator Null (%)	Source Null (%)	P.A. (or Rotation) (deg)	λ (μm)	Reference
HR 5999	5.7 ± 4.6	5.6 ± 2.5	0.1 ± 5.2	−165 (rotation)	11.7	1
	1.1 ± 1.1	5.6 ± 2.5	−4.5 ± 2.7	110 (rotation)	11.7	1
KK Oph	7.5 ± 4.2	5.6 ± 2.5	1.9 ± 4.9	−150 (rotation)	11.7	1
	4.3 ± 2.9	5.6 ± 2.5	−1.3 ± 3.8	120 (rotation)	11.7	1
DK Cha	10.3 ± 4.2	8.4 ± 1.5	1.9 ± 4.4	−170 (rotation)	11.7	1
HD 150193	10.6 ± 2.6	6.9 ± 0.2	3.7 ± 2.6	145 (rotation)	11.7	1
	13 ± 5	13 ± 2	0 ± 5	97	10.3	2
HD 98922	5.9 ± 3.3	24.1 ± 7.6	−18.2 ± 8.3	−40 (rotation)	11.7	1
	15.2 ± 5.8	12.3 ± 3.9	2.9 ± 7.0	−40 (rotation)	10.3	1
HD 104237	9.2 ± 6.7	15.5 ± 1.0	−6.3 ± 6.7	−60 (rotation)	11.7	1
	10.3 ± 1.9	15.4 ± 3.2	−5.1 ± 3.7	−60 (rotation)	10.3	1
51 Oph	11.9 ± 1.1	22.9 ± 10.4	−11.0 ± 10.5	1	11.7	1
	7.3 ± 5.0	22.9 ± 10.4	−15.6 ± 11.5	2	11.7	1
R CrA	19.8 ± 5.1	18.1 ± 2.7	1.7 ± 5.8	1	11.7	1
	26.4 ± 1.9	18.1 ± 2.7	8.3 ± 3.3	2	11.7	1
AB Aur	25.9 ± 1.5	5.1 ± 0.2	20.8 ± 1.5	170	10.3	3
	18.3 ± 1.4	5.1 ± 0.2	13.2 ± 1.4	107	10.3	3
	24.1 ± 2.9	5.1 ± 0.2	19.0 ± 2.9	71	10.3	3
	20.9 ± 1.5	5.1 ± 0.2	15.8 ± 1.5	131	10.3	3
	31.7 ± 3.1	5.1 ± 0.2	26.6 ± 3.1	4	10.3	3
V892 Tau	24.2 ± 2.2	18.5 ± 0.8	5.7 ± 2.3	164	10.3	3
	37.9 ± 7.2	22.0 ± 1.3	15.9 ± 7.3	116	11.7	3
	36.4 ± 0.2	22.0 ± 1.3	14.4 ± 1.3	160	11.7	3
HD 100546	45.5 ± 1.6	8.6 ± 0.1	36.9 ± 1.6	−80 (rotation)	10.3	4
	39.9 ± 7.0	8.6 ± 0.1	31.3 ± 7.0	−50 (rotation)	10.3	4
	41.9 ± 2.8	8.6 ± 0.1	33.3 ± 2.8	−24 (rotation)	10.3	4
	29.8 ± 8.9	8.6 ± 0.1	21.2 ± 8.9	10 (rotation)	10.3	4
	31.6 ± 0.6	12.5 ± 1.8	19.1 ± 1.9	40 (rotation)	10.3	4
	40.0 ± 2.3	6.4 ± 2.4	33.6 ± 3.3	−80 (rotation)	11.7	4
	26.1 ± 2.7	6.4 ± 2.4	19.7 ± 3.6	−50 (rotation)	11.7	4
	37.4 ± 2.5	8.6 ± 2.0	28.8 ± 3.2	−24 (rotation)	11.7	4
	31.8 ± 2.6	8.6 ± 2.0	23.2 ± 3.3	10 (rotation)	11.7	4
	24.3 ± 2.0	9.8 ± 2.2	14.5 ± 3.0	40 (rotation)	11.7	4
	35.5 ± 2.8	5.6 ± 1.8	29.9 ± 3.3	−80 (rotation)	12.5	4
	48.8 ± 1.3	5.6 ± 1.8	43.2 ± 2.2	−50 (rotation)	12.5	4
	30.9 ± 1.7	6.1 ± 0.1	24.8 ± 1.7	−24 (rotation)	12.5	4
	26.4 ± 1.6	6.1 ± 0.1	20.3 ± 1.6	10 (rotation)	12.5	4
	16.3 ± 5.9	10.3 ± 2.1	6.0 ± 6.3	40 (rotation)	12.5	4
HD 163296	12 ± 7	13 ± 2	−1 ± 7	94	10.3	2
	16 ± 2	13 ± 2	3 ± 3	10	10.3	2
HD 179218	16 ± 2	13 ± 2	3 ± 3	162	10.3	2
	14 ± 2	13 ± 2	1 ± 3	87	10.3	2
	10.5 ± 2.4	3.7 ± 0.6	6.8 ± 2.5	50	10.6	1
	8.5 ± 1.8	3.6 ± 0.8	4.9 ± 2.0	60	10.6	1
	7.2 ± 1.2	3.6 ± 0.8	3.6 ± 1.4	99	10.6	1
	11.4 ± 2.5	5.9 ± 1.2	5.5 ± 2.8	103	10.6	1

REFERENCES.—(1) This paper; (2) Hinz et al. 2001; (3) Liu et al. 2005; (4) Liu et al. 2003.

source nulls are included here for the sake of completeness in presenting data. Other negative source nulls are present in the results, but their significance is marginal as the values are negative at less than a 2 σ significance. The large values of calibrator nulls and errors in these cases are likely due to short-lived poor seeing affecting a single observation of the calibrator (two or more observations of the same calibrator are averaged to produce the quoted value for the calibrator null). Again, the inclusion of these results is for the sake of completeness and transparency in our methodology.

3.1. *Simple Disk Models: Assessing Size and Flaring*

In order to infer the size of the emitting region for each resolved object, we use two simple disk models: (1) the intensity of the disk is a Gaussian function with the peak at the center; and (2) the source of the emission is confined to an annulus of uniform intensity around the star. The models are placed at the distance of the object and convolved with the transmission pattern of the interferometer, and a theoretical source null is calculated. The size of the emitting region in the model is adjusted until the results best match the observationally determined source null. Models are fit for each wavelength at which an object was observed. For any object for which we have data at several rotations of the interferometer baseline, we fit a sinusoidal function of the form described in § 2.2 to the S versus P.A. relation determined from our nulling observations. The fitting procedure is described in detail in Liu et al. (2003, 2005).

The extent of the 10 μm emitting region in each of the resolved objects is a powerful tool for determining the physical structure

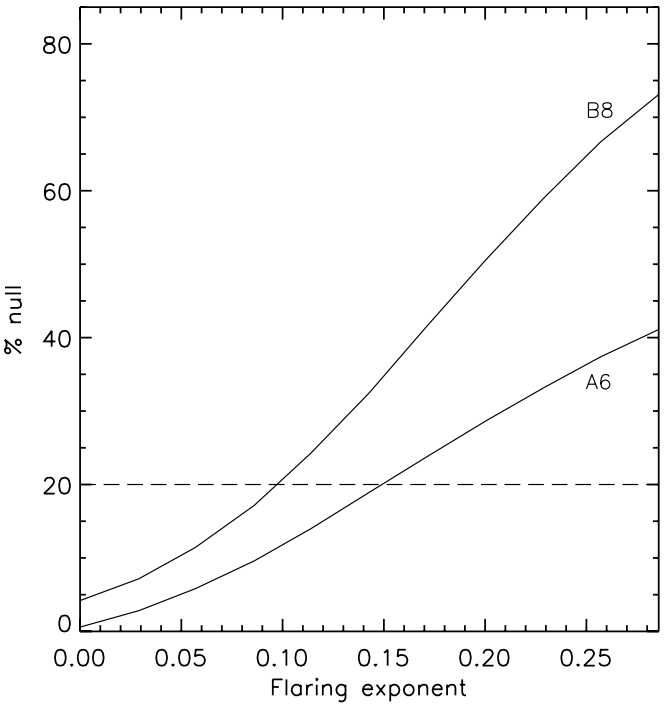

FIG. 1.—Predicted source null vs. degree of flaring. The degree of flaring is represented by varying the exponent of a in CG97 (eq. [10]) from 0 (the flat-disk case) to 2/7 (the vertical hydrostatic equilibrium case). Spectral types A6 and B8 are shown; intermediate types lie between the two curves. The horizontal dashed line represents the median (and mean) source null (20%) for all spatially resolved measurements.

of warm dust in the system. Several factors contribute to the spatial extent of emission. One factor is the degree of disk flaring; thus we explore the effect of flaring on the nulling observations. Another factor affecting the extent of the emitting region is grain size, as larger blackbody grains would tend to result in an emitting region closer to the star, due to the relative efficiency in emission compared to small grains. We also examine the effect of grain size on our observations.

In order to assess the effect that the degree of disk flaring has on the resolvability of a target, we construct a simple face-on flared-disk model based on the model of Chiang & Goldreich (1997, hereafter CG97). In our model we vary the degree of flaring by adjusting the power-law dependence of the flaring term, H/a (eq. [10] of CG97, where H is the height of the disk above the midplane and a is the radial separation between the star and a point on the midplane of the disk). The exponent of a is varied from 0 (the flat-disk case, i.e., constant H/a) to 2/7 (the vertical hydrostatic equilibrium case, i.e., $H/a \sim a^{2/7}$). Other parameters assumed in the CG97 model include a dust mass of 1% of the gas mass, uniformly mixed, a grain size of 0.1 μm, and a mass density of 2 g cm^{-3}. The CG97 model was used to determine the brightness from a hypothetical disk, using canonical stellar parameters (effective temperature, mass, radius, and luminosity) (Cox 2000) appropriate for the spectral types of the targets' parent stars, while varying the amount of flaring in the disk. This brightness signature is then convolved with the transmission function of the interferometer to predict the source nulls expected for varying degrees of flaring. Figure 1 shows the predicted values of the source null as a function of the degree of flaring (represented by the value of the exponent of a) for a range of spectral types. We see that the model predicts very large source nulls (40%–75%) for the maximally flared disks in all cases. This holds true also for the outer part of the model (Dullemond et al. 2001, eq. [5]), which predicts flaring as the disk emerges from the shadowed region. The largest source null for our resolved objects approaches 40% for HD 100546, a B9 star. Thus, it appears that if one considers flaring as the only factor affecting the observed source null, none of the objects display flaring to the degree of the hydrostatic equilibrium case. It is a possibility that this is an indication that the warm dust may be in a flatter distribution than expected (possibly due to dust settling toward the disk midplane). However, one must keep in mind that other factors (such as the orientation of the dust relative to the rotation of the interferometer baseline) can have a significant effect on the source null.

TABLE 4
BEST-FIT MODELS

Name	λ (μm)	Gaussian FWHM (AU)	Ring Diameter (AU)	Flaring Exponent[a]	Reference
HR 5999.....	11.7	<19	<26	<0.06	1
KK Oph.....	11.7	<14	<19	<0.06	1
DK Cha.....	11.7	<17	<23	<0.05	1
HD 150193	11.7	<12	<16	<0.01	2
HD 98922	11.7	<48	<68	<0.04	1
HD 104237	11.7	<12	<16	<0.07	1
51 Oph	11.7	<17	<23	<0.08	1
R CrA.....	11.7	15 ± 4	20 ± 4	0.02–0.07	1
AB Aur	10.3	27 ± 3	30 ± 3	0.1–0.15	3
V892 Tau	10.3	14 ± 2	20 ± 3	0.05–0.15	3
	11.7	23 ± 5	31 ± 6	0.05–0.15	3
HD 100546	10.3	24 ± 3	26 ± 3	0.08–0.18	4
	11.7	25 ± 3	27 ± 3	0.07–0.18	4
	12.5	30 ± 3	33 ± 3	0.02–0.2	4
HD 163296	11.7	<11	<15	<0.08	2
HD 179218	10.6	20 ± 4	27 ± 5	0.01–0.05	1

[a] In the range 0 to 2/7; see § 3.1.

REFERENCES.—(1) This paper; (2) Hinz et al. 2001; (3) Liu et al. 2005; (4) Liu et al. 2003.

Spatial information about the emission regions surrounding these stars is also important in breaking degeneracies in interpreting the SEDs with regard to grain size. For example large grains, with sizes similar to the wavelength of emission, at closer separations from the star can manifest themselves in the same way as small, ISM-sized grains in a more extended distribution. In the model based on CG97 described above, the assumed grain size is 0.1 μm, or ISM-sized grains. Thus for resolved objects, if grain sizes are actually larger than the assumed size, this would require a greater degree of flaring than the actual values calculated with the model, in order to account for the same level of resolved flux. When comparing the relative effect that grain size and flaring have on the temperature profile of the dust, we see that varying the flaring has a greater effect on the power-law dependence of the effective temperature versus separation from the star. Increasing the flaring from a flat distribution to a flared distribution (at vertical hydrostatic equilibrium) results in a change from a $T \sim r^{-0.75}$ relation to $T \sim r^{-0.4}$, and to a change in source null of 40%–70%, depending on the luminosity of the star.

Table 4 summarizes the sizes and flaring parameters that best fit the nulling data, with the errors representing the error in source null shown in Table 3. For unresolved objects, a maximum size for the emitting region is shown, calculated using the error in the source null.

3.2. *Notes on Resolved Objects*

HD 100546.—This object is perhaps the oldest star in our sample, with an estimated age exceeding 10 Myr (see footnote b,

Table 1). Large fractions of crystalline silicates suggest an evolved disk and evidence of a giant protoplanet in the system (Bouwman et al. 2003; Malfait et al. 1998; Waelkens et al. 1996). HD 100546 was resolved with non-AO observations (both nulling interferometric and direct imaging) at Magellan I. Nulling observations at 10.3, 11.7, and 12.5 μm show evidence for an inclined disk with an orientation of 45° from face-on and a radius of about 12 AU, with a slightly larger size resulting from the ring model (Liu et al. 2003). Direct imaging at 18.0 and 24.5 μm also shows resolved emission at a greater separation (15–20 AU) from the star and verifies the orientation of the dust disk. We find that the relative sizes of the 10 and 20 μm emission to not agree with the $T \sim r^{-0.5}$ relation for a continuous flared disk (CG97). Instead, a disk with a large inner clearing ($r < 10$ AU) would result in the 10 μm emission being detected at a greater separation than expected, explaining the relative sizes of the emission at different wavelengths. This inner clearing could be the result of the formation of a giant planet. Further discussion of this model can be found in Liu et al. (2003). Here we also consider the possibility that the relative sizes of the emission regions may be a consequence of an inner self-shadowed region in the disk. In the models of Dullemond et al. (2001) one sees that for the shadowing to extend out to the radii of the detected 10 μm emission (>10 AU), the height of the inner rim would have to be enhanced relative to the height expected, due to direct normal-incidence radiation. If this were the case, the models also predict a significant decrease in the strength of the 10 μm emission feature. As HD 100546 shows a strong emission feature, it appears that self-shadowing is not a significant effect in determining the relative sizes of the resolved emission regions in this system. The relatively large source nulls of HD 100546 suggest a moderate degree of flaring even with the smallest grain sizes. This result supports the fact that self-shadowing is not a factor in the regions we observe and is also in agreement with the SED analysis of Bouwman et al. (2003), which infers that the vertical height of the disk must be enhanced at ~10 AU.

AB Aur.—The age of AB Aur is estimated to be significantly younger than HD 100546, with its SED showing no evidence for crystalline silicates (M01). Observations of AB Aur at 10.3 μm (*N* band) with AO were taken at five different rotations of the interferometer baseline and, like HD 100546, show a variation consistent with the presence of an inclined disk. A fit to the data results in a disk radius of 12–15 AU, with the smaller sizes in this range from the Gaussian disk model, and the larger sizes a result of fitting to the ring model. These sizes are consistent with a recent mid-IR study by Marinas et al. (2006). A disk inclination of 45°–65° and a major-axis P.A. of 15°–45° are also inferred (Liu et al. 2005). The orientation of the disk (inclination, P.A.) derived from these mid-IR observations differs from from that in several near-IR and millimeter observations previously completed (Fukagawa et al. 2004; Eisner et al. 2003; Millan-Gabet et al. 2001; Mannings & Sargent 1997). This suggests that the circumstellar environment may be more complex than a simple disk structure. However, the sizes of the disk at different wavelengths from this and the aforementioned studies, in addition to the mid-IR study of Chen & Jura (2003), indicate that the wavelength versus size relation is consistent with a temperature profile of $T \sim r^{-0.5}$ expected from a flared disk. A full discussion can be found in Liu et al. (2005). From relatively large source nulls and the fit to the flaring model, a moderate amount of flaring can be inferred.

HD 179218.—This is one of the most distant objects in our sample (244 pc; Perryman et al. 1997), and its SED shows significant levels of crystalline silicates (M01). Initial observations without AO failed to resolve this star, resulting in a source null of 3% ± 3% at a P.A. of 162° (Hinz et al. 2001). Given the greater precision with the use of AO, follow-up observations were made in 2005 June. These follow-up observations have positively detected resolved emission at levels from 3% to 7% (0.7 to 1.6 Jy). A plot of source null versus P.A. is shown in Figure 2. An average of the source nulls implies a FWHM of 20 ± 4 AU for the Gaussian disk model or a diameter of 27 ± 5 AU for a ring distribution of dust. The low source nulls may also suggest flaring in the dust that is small, significantly less than in the vertical hydrostatic equilibrium case. The *S* versus rotation relation does not show significant variation, consistent with circular symmetry, although significant inclinations cannot be ruled out, as a hypothetical disk with an inclination of 45° results in a variation in the source null of about 3%, within the errors of the measurement. The presence of significant silicate emission in the *ISO* spectra of M01 also seems to rule out a large inclination for the object, which would result in a drop-off in emission intensity at wavelengths shorter than about 10 μm (Chiang & Goldreich 1999). However, we do not make any definite conclusions regarding the spatial orientation of the dust.

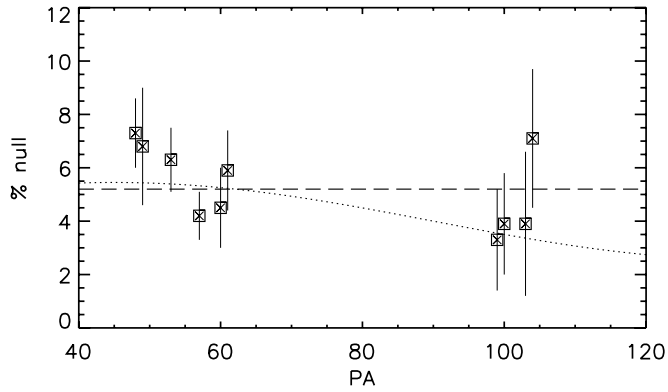

FIG. 2.—Source null vs. P.A. for HD 179218, spatially resolved with AO observations. The horizontal dashed line is the mean of the measurements, and expected signature (no variation in null vs. P.A.) from a circularly symmetric source. The dotted line shows the expected variation in null for a 20 AU diameter, Gaussian intensity distribution inclined at 45°.

V892 Tau.—Observations at 11.7μm without AO, and at 10.3μm using AO, show resolved emission at a level of about 3 Jy from this Herbig Ae source. The emission is detected at a P.A. of 164°, but no information can be derived as to the overall orientation of the emission, as data were taken at only one rotation. Using an average of the source nulls obtained in the two data sets at 11.7 μm and assuming a Gaussian intensity distribution for the dust, the FWHM is 18–28 AU. The ring distribution yields a diameter of 25–37 AU. At 10.3 μm, these sizes are 12–16 and 17–23 AU, respectively. The relative sizes of the emission at the two wavelengths is consistent within errors to the expected $T \sim r^{-0.5}$ relation for a CG97 flared disk, assuming purely thermal emission. Signs of flaring can also be inferred from the higher level of resolved emission in the 11.7 μm observations but, when considering flaring as the sole factor affecting the extent of the emission region, suggest that the dust lies in a flatter distribution than in the vertical hydrostatic equilibrium case, although this may also be an indication of larger grains.

R CrA.—This object was observed without AO at Magellan I and shows marginal evidence for resolved emission. The object was observed at two rotations of the interferometer, and one of the two rotations yielded a positive detection at the 2 σ level. The level of resolved emission is 8% and suggests a spatial extent for the dust of 15 ± 4 AU using a Gaussian dust distribution and 20 ± 4 AU using a ring distribution. As with V892 Tau, the

source nulls are possibly indicative of less flaring than a hydrostatic equilibrium situation would expect, or larger grains than ISM sizes.

4. DISCUSSION

4.1. *Trends in Resolved Objects*

In selecting our HAe targets, we included objects with a range of spectral types and ages, in the hope that any evidence of evolution in the PMS environment, or differences in the circumstellar region due to the stellar mass of the parent star, could be probed. However, we have found that the resolved objects in our sample appear to have a range of stellar characteristics. The resolved objects have spectral types ranging from late B type (HD 100546 and HD 179218) to A6 (V892 Tau), and ages ranging from approximately 0.1 (HD 179218) to >10 Myr (HD 100546). Therefore, there seems to be no distinguishing characteristic between unresolved and resolved sources in terms of age or spectral type. A plot of the inferred disk size (see § 3.1) versus the stellar age (for those objects with age determinations in the literature) is shown in Figure 3 (*top*) and shows no obvious trend. This could be due to either (1) errors in age estimates for these stars or (2) the fact that time is not the sole or dominant factor affecting disk evolution.

An analysis of the SEDs of the observed stars, however, does suggest a trend in the resolved objects. M01 categorizes Herbig stars into two major groups: group I with large amounts of mid-infrared excess, and group II with moderate quantities of mid-IR excess, descending at longer wavelengths. For those objects with classifications in the literature, we find that two out of three group I objects were resolved in our initial observations (we do not include HD 179218 as a resolved object here since it was unresolved in our initial, non-AO observations), while zero of five group II objects showed resolved emission. This trend is evident in a plot of disk size versus the submillimeter SED slope (Fig. 3, *middle*), which M01 find correlates well with the mid-IR SED grouping of the star and could be considered a surrogate for the evolutionary state of the disk. Objects with steeper submillimeter slopes (index < -3) appear to have larger, resolvable disks. A calculation of the Kendall τ correlation coefficient (Press et al. 1992) for the SED slope versus disk size relation yields a correlation probability of 94%, whereas the stellar age versus disk size relation discussed in the previous paragraph yields a correlation probability of 43%. We also see a correlation (87% probability) between the fractional IR luminosity (calculated by M01) and the disk size (Fig. 3, *bottom*).

M01 attributes the difference in the SED between these two groups to disk geometry, with group I objects displaying a significant amount of flaring outside the inner disk, while disks in a group II source have less flaring, a result of shielding from an optically thick inner disk or perhaps self-shadowing from a puffed-up inner wall (Dullemond et al. 2001). It is conceivable that the flaring in the group I objects results in the disk intercepting more radiation at greater radii, making it easier to spatially resolve the dust disk. M01 correlate the amount of mid-IR excess to the scale height of the disk, with greater excesses as a result of more substantial flaring in the disk, consistent with the observed trend in our survey. In contrast, the 10 μm emission in the group II shadowed disk will be confined to the inner few AU, making it more difficult for resolved emission to be detected. Thus our results are in good agreement with those of Leinert et al. (2004), who found that the mid-IR emitting regions were larger for the redder, group I objects.

Despite this line of reasoning, there is reason to be cautious before attributing the characteristics of the SED groupings to an all-

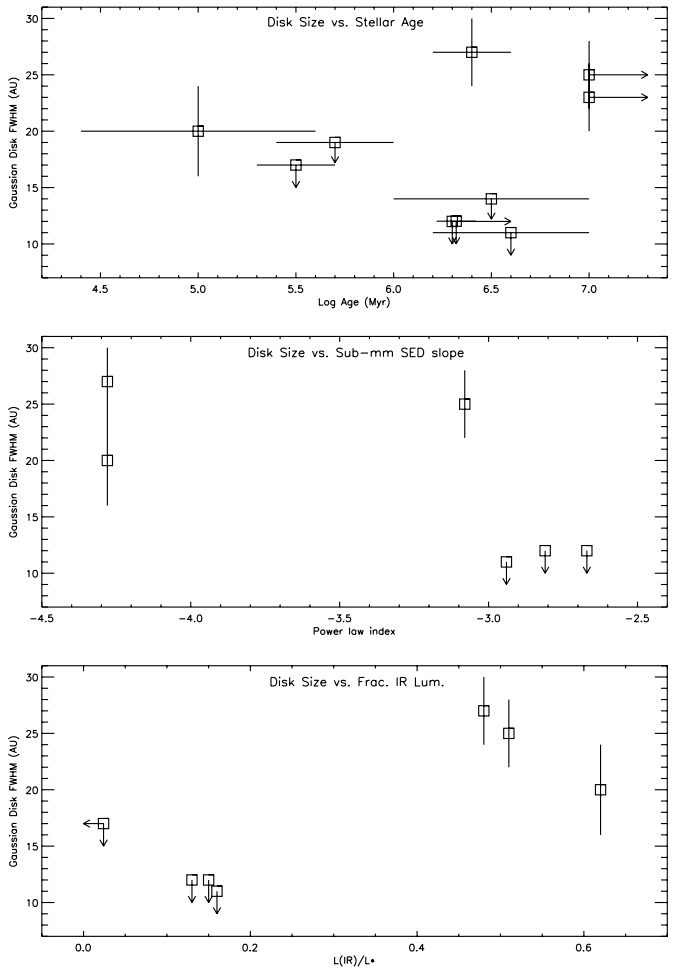

FIG. 3.— *Top*: Disk size (inferred from fitting a Gaussian intensity distribution to the source null) vs. stellar age (for 10 objects with age determinations in the literature) for our sample. Sizes plotted are derived from the 11.7 μm observations except AB Aur (10.3 μm) and HD 179218 (10.6 μm). No clear age trend is apparent in the data. *Middle*: Disk size vs. submillimeter SED slope (for the six objects with values determined in M01). Objects with steeper SEDs in the submillimeter (index < -3.0) correlate with group I objects and appear to have larger, resolvable disks. *Bottom*: Disk size vs. fractional IR luminosity (seven objects from M01). A larger IR excess correlates to larger disk size. Given the poor constraint on the distance to HD 98922, it is not included in any of the plots.

encompassing physical model. M01 make the assertion that group II objects show evidence that they are more evolved, due to large grain sizes. This would seem to imply that older objects are less likely to be resolved than younger ones, if time is the dominant factor in the evolution of these systems. In our sample, we do not find any trends in resolved objects with age. This would imply that either the age of the system is a poor indicator of the evolutionary state of the system, or that the ages attributed to the stars are in error. We can gain insight into this issue by comparing HD 100546 and AB Aur, the two most conclusively resolved objects. By comparing observations at different wavelengths for each object from this and other studies, we find that the temperature versus radius relation for the stars is dramatically different. The temperature profile suggests that AB Aur and HD 100546 do not have similar circumstellar environments despite the similarity in the 10 μm resolved emission. The former is consistent with the $T \sim r^{-0.5}$ relation expected from a simple flared disk (CG97), while the latter shows evidence for an inner disk gap (see details in § 3.2 and Liu et al. 2003). Thus, the evidence here suggests that our ability to resolve an object may be due to different

circumstances in each system and cannot necessarily be attributed to similar physical models.

5. SUMMARY AND CONCLUSIONS

We have carried out 10 μm nulling interferometric observations of 13 Herbig Ae stars and reach the following primary conclusions:

1. We have conclusively resolved warm dust surrounding three objects, HD 100546, AB Aur, and HD 179218, the latter previously unreported. Both HD 100546 and AB Aur show significant variation in source null versus P.A., which is evidence for an elongated structure such as an inclined disk (Liu et al. 2003, 2005). HD 179218 was resolved in recent (2005 June) observations with AO, and preliminary results suggest little variation of null versus P.A., consistent with an axisymmetric distribution (such as a face-on disk) for the dust, although a significant inclination cannot be ruled out given the errors in the measurement.

2. We have found evidence for resolved emission around an additional two HAe stars, V892 Tau and R CrA. Both the sources show resolved emission at a level of a few percent of the unresolved flux at 10 μm.

3. The spatial extent of the emitting region in the resolved systems ranges from 15 to 30 AU in diameter, assuming two models: a Gaussian disk and a ring.

4. Both SED slope and fractional IR luminosity appear to be good indicators of the spatial extent of circumstellar dust. Although our sample size is small, it appears that M01 group I objects are more resolvable than group II objects, a result consistent with Leinert et al. (2004). This trend is evident in the correlation between disk size and submillimeter spectral slope as well as disk size and fractional IR luminosity.

5. There is a lack of correlation in disk size versus stellar age, perhaps due to uncertainty in age determination and/or the fact that time is not the sole or dominating factor in disk evolution.

6. Using a model based on CG97, we evaluate the effect of disk flaring on the resolvability of the objects. We find that a hypothetical object with flaring consistent with vertical hydrostatic equilibrium would produce a very large source null in all objects. The fact that the source nulls observed in these objects is not that large suggests that flaring does not impact the resolvability of the objects as much as expected. In this latter case, an alternative explanation for the correlation between the SED groups and resolvability must be determined. One possible explanation for this is the grain size. With grain sizes larger than ISM sizes, flaring must be enhanced to account for the same amount of resolved flux.

7. Follow-up AO observations should be made on all objects not yet observed with AO, in order to better constrain the limits or possibly detect their spatial extent. Observations of group Ib objects, those without strong 10 μm silicate emission, would also be interesting for assessing any correlation between the presence of these emission lines and the spatial resolvability of the objects, and would further constrain the distribution and orientation of the disks.

W. M. L. was supported under a Michelson Graduate Fellowship. E. E. M. is supported through a Clay Postdoctoral Fellowship from the Smithsonian Astrophysical Observatory. We are grateful to the operators and staffs at the MMT and Magellan Observatories for their support of our observations. We thank A. Breuninger and B. Duffy for technical support of BLINC-MIRAC. The authors also thank J. Najita and the anonymous referee for helpful comments in the revision of this paper. P. H. and M. R. M. acknowledge support from the NASA Astrobiology Institute. BLINC was developed under a grant from NASA/JPL. The MMT AO system was developed with support from the Air Force Office of Scientific Research. This work made use of the SIMBAD database.

REFERENCES

Bouwman, J., de Koter, A., Dominik, C., & Waters, L. B. F. M. 2003, A&A, 401, 577
Bracewell, R. N. 1978, Nature, 274, 780
Brusa, G., et al. 2003, Proc. SPIE, 4839, 691
Calvet, N., Patino, A., Magris, G. C., & D'Alessio, P. 1991, ApJ, 380, 617
Chen, C. H., & Jura, M. 2003, ApJ, 591, 267
Chiang, E. I., & Goldreich, P. 1997, ApJ, 490, 368 (CG97)
———. 1999, ApJ, 519, 279
Cox, A. N. 2000, Allen's Astrophysical Quantities (4th ed.; New York: AIP)
de Zeeuw, P. T., Hoogerwerf, R., de Bruijne, J. H. J., Brown, A. G. A., & Blaauw, A. 1999, AJ, 117, 354
Dullemond, C. P. 2002, A&A, 395, 853
Dullemond, C. P., Dominik, C., & Natta, A. 2001, ApJ, 560, 957
Eisner, J. A., Lane, B. F., Akeson, R. L., Hillenbrand, L. A., & Sargent, A. I. 2003, ApJ, 588, 360
Fukagawa, M., et al. 2004, ApJ, 605, L53
Hamaguchi, K., Yamauchi, S., & Koyama, K. 2005, ApJ, 618, 360
Hartmann, L., Kenyon, S. J., & Calvet, N. 1993, ApJ, 407, 219
Hillenbrand, L. A., Strom, S. E., Vrba, F. J., & Keene, J. 1992, ApJ, 397, 613
Hinz, P. M. 2001, Ph.D. thesis, Univ. Arizona
Hinz, P. M., Hoffmann, W. F., & Hora, J. L. 2001, ApJ, 561, L131
Hoffmann, W. F., Hora, J. L., Fazio, G. G., Deutsch, L. K., & Dayal, A. 1998, Proc. SPIE, 3354, 647
Kenyon, S. J., & Hartmann, L. 1987, ApJ, 323, 714
Lada, C. J., & Adams, F. C. 1992, ApJ, 393, 278
Leinert, C., et al. 2004, A&A, 423, 537
Liu, W. M., Hinz, P. M., Hoffmann, W. F., Brusa, G., Miller, D., & Kenworthy, M. A. 2005, ApJ, 618, L133
Liu, W. M., Hinz, P. M., Meyer, M. R., Mamajek, E. E., Hoffmann, W. F., & Hora, J. L. 2003, ApJ, 598, L111
Malfait, K., Waelkens, C., Waters, L. B. F. M., Vandenbussche, B., Huygen, E., & de Graauw, M. S. 1998, A&A, 332, L25
Mamajek, E. E., Meyer, M. R., & Liebert, J. 2002, AJ, 124, 1670
Mannings, V., & Sargent, A. I. 1997, ApJ, 490, 792
Marinas, N., et al. 2006, ApJ, 653, 1353
Marsh, K. A., Van Cleve, J. E., Mahoney, M. J., Hayward, T. L., & Houck, J. R. 1995, ApJ, 451, 777
Meeus, G., Waters, L. B. F. M., Bouwman, J., van den Ancker, M. E., Waelkens, C., & Malfait, K. 2001, A&A, 365, 476 (M01)
Millan-Gabet, R., Schloerb, F. P., & Traub, W. A. 2001, ApJ, 546, 358
Miroshnichenko, A., Ivezić, Ž., Vinković, D., & Elitzur, M. 1999, ApJ, 520, L115
Natta, A., Grinin, V., & Mannings, V. 2000, in Protostars and Planets IV, ed. V. Mannings, A. Boss, & S. S. Russell (Tucson: Univ. Arizona Press), 559
Perryman, M. A. C., et al. 1997, A&A, 323, L49
Press, W. H., Teukolsky, S. A., Vetterling, W. T., & Flannery, B. P. 1992, Numerical Recipes (2nd ed.; Cambridge: Cambridge Univ. Press)
The, P. S., de Winter, D., & Perez, M. R. 1994, A&AS, 104, 315
van den Ancker, M. E., de Winter, D., & Tjin A Djie, H. R. E. 1998, A&A, 330, 145
Vinković, D., Ivezić, Ž., Jurkić, T., & Elitzur, M. 2006, ApJ, 636, 348
Vinković, D., Ivezić, Ž., Miroshnichenko, A. S., & Elitzur, M. 2003, MNRAS, 346, 1151
Waelkens, C., et al. 1996, A&A, 315, L245